Journal of Materials Chemistry C

Antiferroelectric-to-ferroelectric phase transition in hexagonal rare-earth iron oxides

Journal:	*Journal of Materials Chemistry C*
Manuscript ID	TC-ART-12-2021-005944.R2
Article Type:	Paper
Date Submitted by the Author:	02-Mar-2022
Complete List of Authors:	Chen, Binjie; Hokkaido University Hasegawa, Tetsuya; The University of Tokyo Ohta, Hiromichi; Hokkaido University, Research Institute for Electronic Science; Hokkaido University Katayama, Tsukasa; Hokkaido University, research institute for electronic science

Antiferroelectric-to-ferroelectric phase transition in hexagonal rare-earth iron oxides

Binjie Chen[1], Tetsuya Hasegawa[2], Hiromichi Ohta[3], Tsukasa Katayama[3,4]*

[1]Graduate School of Information Science and Technology, Hokkaido University, N14W9, Kita, Sapporo 060-0814, Japan.

[2]Department of Chemistry, The University of Tokyo, Bunkyo, Tokyo 113-0033, Japan.

[3]Research Institute for Electronic Science, Hokkaido University, N20W10, Kita, Sapporo 001-0020, Japan.

[4]JST-PRESTO, Kawaguchi, Saitama 332-0012, Japan

*Corresponding author: katayama@es.hokudai.ac.jp

Abstract

Ferroic oxides often exhibit exotic behavior, accompanied by phase transitions. Hexagonal rare-earth iron oxides (*h*-*R*FeO_3), a promising multiferroic system, were reported to exhibit ferroelectricity (FE) when the lattice parameter ratio (*c*/*a*) exceeded 1.93 and antiferroelectricity (AFE) when *c*/*a* equaled to 1.89. Although the AFE–FE phase boundary in *h*-*R*FeO_3 systems is assumed to exist at *c*/*a* ≈ 1.9, the phase transition has not been observed so far due to the lack of samples with such *c*/*a* ratio. In this study, we show AFE–FE phase transition in *h*-*R*FeO_3 films, where *R* = Dy. We fabricated *h*-$DyFeO_3$ films with *c*/*a* ratios of 1.90–1.92 by controlling the film thicknesses. The *h*-$DyFeO_3$ films with *c*/*a* of 1.91 exhibited AFE at temperatures below 200 K and FE at temperatures up to 300 K. The phase transition temperature (T_p) was modulated by the *c*/*a* ratio. The films also underwent an AFE–FE phase transition upon adjusting the frequency of voltage applied at the T_p. We discuss the possible origin of the AFE–FE phase transition from the viewpoint of the migration length of the FE domain wall motion.

1. Introduction

Phase transition in ferroic materials provides fascinating features, which would achieve low-energy-consumption devices and high-density memory storage devices. For example, giant permittivity arising from a ferroelectric (FE)-to-paraelectric transition has been applied to various devices, such as capacitors, antennas, and phase shifters [1-3]. On the other hand, electric field (*E*)-induced magnetization change is realized, at room temperature, by using a ferromagnetic (FM)-to-paramagnetic transition [4,5]. In such a conventional ferro-to-para transition, spontaneous polarization or magnetization drops to zero at the transition temperature. In contrast, in the recently discovered antiferro-to-ferro transition, the spontaneous polarization/magnetization value increases sharply with the temperature (*T*) associated with the phase transition. Examples of AFE-to-FE transition materials include $Hf_{1-x}Zr_xO_2$ [1,6], $PbZrO_3$ [7], $Bi_{1-x}R_xFeO_3$ (*R* is a rare-earth element) [8], and hexagonal (*h*-) $RMnO_3$ [9-11], while examples of antiferromagnetic to FM transition materials include FeRh [12,13], $Sr_xR_{1-x}MnO_3$ [14], and $RBaCo_2O_{5.5}$ [15,16]. These phase transitions also provide unique properties, such as *E*-tunable large pyroelectric and electrocaloric effects near room temperature [17,18], giant magnetoresistance [15], a sign change in magnetocapacitance [10], and current-induced phase transition [19]. However, the limited number of materials exhibiting antiferro-to-ferro phase transition properties necessitates the discovery of new systems.

h-$RFeO_3$ materials, exhibiting FE and magnetic orders simultaneously, have been intensively studied as promising multiferroic materials owing to their high FE ordering temperatures and strong coupling between magnetic and FE domains [20-23]. The FE polarization is derived from the geometric tilting of FeO_5 bipyramids and the corresponding displacement of the *R* ion [21]. Because this tilting is related to the lattice parameters, the FE properties can be modulated by changing the *c*/*a* ratio [24]. For example, *h*-$RFeO_3$ exhibits FE behavior when *c*/*a* exceeds 1.93 [25-29], while it shows AFE behavior when *c*/*a* = 1.89 [24]. However, the boundary between the AFE and FE phases remains unknown, resulting in an absence of AFE–FE phase transition in one crystal of *h*-$RFeO_3$. For attaining

AFE–FE phase transition in a multiferroic *h*-*R*FeO_3 system, we systematically investigated ferroelectric properties of *h*-$DyFeO_3$ epitaxial films by tuning *c*/*a* ratio by changing the thickness. As a result, we successfully observed *T*-induced AFE–FE phase transition phenomena. The variable *c*/*a* (1.90–1.92) is intermediate between those of previously reported AFE and FE *h*-*R*FeO_3. The 38-nm-thick *h*-$DyFeO_3$ (*c*/*a* = 1.91) underwent AFE–FE phase transition at 200 K. The phase transition temperature can be modified by changing the *c*/*a* and/or frequency of the applied voltage.

2. Experimental

h-$DyFeO_3$ films and indium tin oxide (ITO) bottom electrode layers were fabricated on (111)-oriented yttria-stabilized zirconia (YSZ) substrates by pulsed laser deposition (PLD), where a KrF excimer laser (λ = 248 nm) was used to irradiate on ceramic ITO and $DyFeO_3$ targets. The $DyFeO_3$ target was prepared by solid-state reaction techniques with Dy_2O_3 (99.9%) and α-Fe_2O_3 (99.9%) powders. The stoichiometrically mixed powder was calcined at 1200 °C for 48 hours, mechanically pressed into a pellet and sintered at 1400 °C for 12 hours. Epitaxial ITO layers were first deposited on the YSZ substrate at 900 °C in an oxygen atmosphere (partial pressure of oxygen (P_{O2}) = 2×10^{-3} Pa), and then the *h*-$DyFeO_3$ film was heteroepitaxially grown on the ITO/YSZ substrate at 800 °C under a P_{O2} of 4 Pa [30,31]. After the deposition, the film is naturally cooled at P_{O2} of 4 Pa. The film thickness and crystal structure were determined using high-resolution X-ray diffraction (XRD, ATX-G, Rigaku Co.) analysis with Cu $K\alpha_1$ (λ = 0.15406 nm) radiation. Chemical composition difference between the films was analyzed by employing scanning electron microscope−energy dispersive X-ray spectroscopy (SEM−EDS). The ferroelectric properties of the *h*-$DyFeO_3$ films were analyzed using a ferroelectric tester (Multiferroic II Ferroelectric Tester, Radiant Technologies Inc.). A 100-μm-diameter Pt electrode, used as the top electrode, was deposited by electron beam evaporation. The measurements were performed at variable temperatures between 14 and 300 K. Atomic force microscopy (AFM, MFP-3D Origin, Oxford) was used to observe the topographic microscopy image and the

piezoresponse force microscopy image.

3. Results and discussion

Figure 1(a) and S1 shows the out-of-plane XRD patterns of the 26-, 38-, and 58-nm-thick *h*-$DyFeO_3$ films grown on ITO / (111) YSZ substrates. The diffraction peaks at $q_z/2\pi$ = 1.70, 3.37, and 3.43 nm^{-1} correspond to the 002 *h*-$DyFeO_3$, 111 YSZ, and 222 ITO peaks, respectively [24], indicating that *c*-axis-oriented *h*-$DyFeO_3$ films were successfully prepared on (111) ITO epitaxial bottom electrodes. The 001 *h*-$DyFeO_3$ peaks were shifted slightly to lower angles with increasing thickness; the lattice parameter *c* monotonically increases from 11.74 to 11.87 Å with increasing the thickness from 26 to 58 nm (Fig. 1(b)). Notably, ϕ-scan measurements revealed that heteroepitaxial growth occurred in all *h*-$DyFeO_3$ films (Fig. S2). To evaluate the in-plane lattice parameter *a*, in-plane XRD measurements were performed along the [11-2] YSZ direction (Fig. S3). From the 110 and 220 diffraction peaks, the lattice parameter *a* of the films was calculated to be almost independent of the thickness (6.18 Å). Depending on the thickness, the *c*/*a* ratio was varied from 1.90 to 1.92 (Fig. 1(c)), which was intermediate between those of previously reported AFE (*c*/*a* = 1.894) and FE (*c*/*a* ≥ 1.933) *h*-*R*FeO_3 [23-29]. It was also indicated that the volume of the unit cell increased with increasing thickness. Figure S5 shows EDS spectra of the films. The integral area ratio of Dy Mα to Fe Lα peaks was 2.498, 3.115 and 3.242 for the 26-, 38-, and 58-nm-thick films, respectively, suggesting that Dy/Fe composition ratio increases with increasing the thickness. Such thickness dependence of composition difference was also observed in other oxide films such as $CuFeO_2$ [32] and $Ba_{1-x}Sr_xTiO_3$ [33] due to the weakening of substrate strain or clamping effect with increasing thickness. It was reported that *c*-axis length of isostructural *h*-$LuFeO_3$ increase with increasing Dy/Fe composition ratio [34,35]. Thus, the increase of *c*-axis length in the *h*-$DyFeO_3$ films with increasing thickness is probably derived from an increase in the Dy/Fe composition ratio.

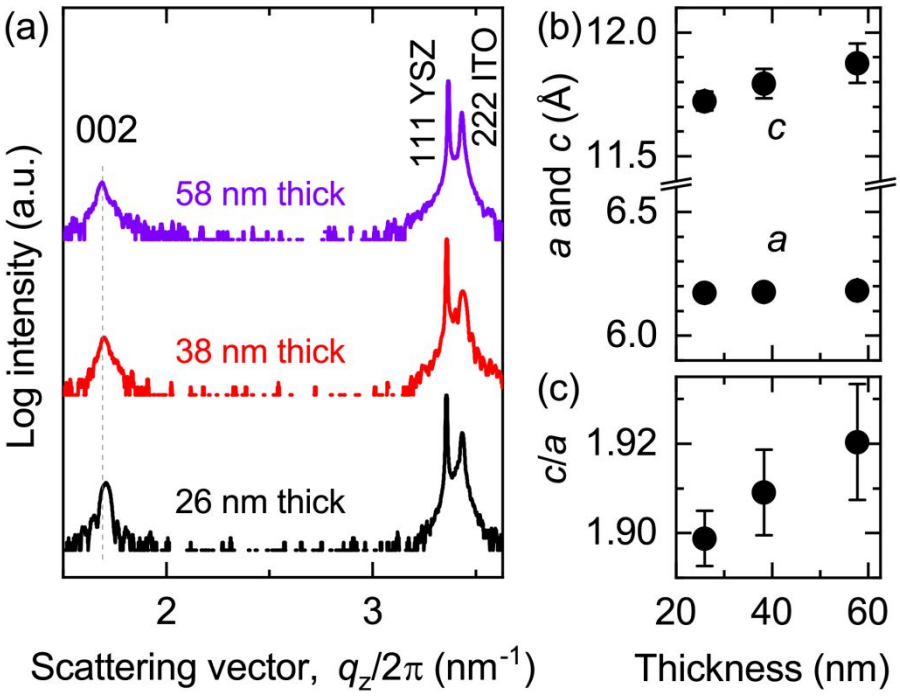

Figure 1. (a) Out-of-plane XRD patterns, (b) lattice constants and (c) *c*/*a* of the *h*-$DyFeO_3$ films as a function of thickness.

Figure 2 shows the polarization and current versus electric field (*P*–*E* and *I*–*E*) curves for the 38-nm-thick *h*-$DyFeO_3$ film. The measurements were conducted at 14–300 K at a frequency of 10 kHz. At $T \leq 175$ K, the *P*–*E* curves exhibited double-hysteresis loops (Fig. 2(a)). In addition, two positive and two negative peaks were observed in the *I*–*E* curve (Fig. 2(b)). These results indicated that the *E*-induced transition from nonpolar to polar states occurs at E_F and returns to a nonpolar state at E_A, i.e., the film exhibits AFE behavior at $T \leq 175$ K. On the other hand, at $T \geq 225$ K, the *P*–*E* curves of the film show single-hysteresis loops (Fig. 2(c)) and the *I*–*E* curves have only one pair of peaks corresponding to coercive *E* (E_c) (Fig. 2(d)), indicating that the film showed FE behavior at $T \geq 225$ K. Therefore, we can conclude that the film underwent a *T*-induced AFE–FE transition.

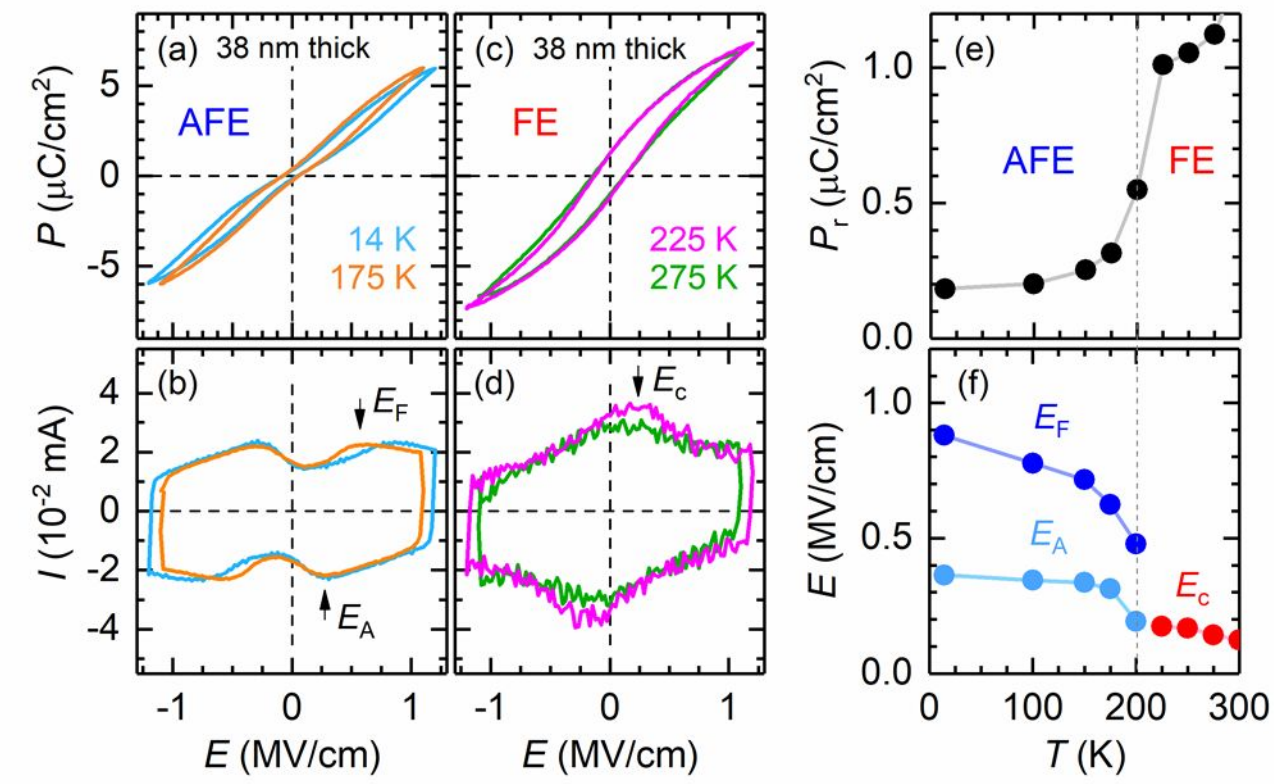

Figure 2. *P*–*E* and *I*–*E* curves for the 38-nm-thick *h*-$DyFeO_3$ film at (a, b) 14, 175, (c, d) 225, and 275 K at 10 kHz. *T* dependence of (e) P_r and (f) E_F, E_A, and E_c for the film with maximum applied *E* of 1.1 MV/cm. The dashed line indicates the boundary between the AFE and FE phases.

Figure 2(e) shows the temperature (*T*) dependence of the remnant polarization (P_r) for the 38-nm-thick film. The P_r value is 0.2–0.3 μC/cm² at $T \leq 175$ K, while it increases to >1 μC/cm² at $T \geq$ 225 K associated with AFE–FE transition. Figure 2(f) shows the E_F, E_A, and E_c values for the film. The E_A and E_F values decrease with increasing *T* and disappear at 225 K, while E_c appears at 225–300 K. From these results, we can conclude that the phase transition occurs at ~200 K.

Figure 3 shows frequency dependence of the *P*–*E* and *I*–*E* curves for the 38-nm-thick *h*-$DyFeO_3$ film at the phase transition temperature of 200 K. When the frequency is 1 kHz, the film shows a single-hysteresis loop in the *P*–*E* curve and a single pair of peaks in the *I*–*E* curve (Fig. 4(a)). On the other hand, at 100 kHz, a double-hysteresis loop and two pairs of peaks appear in the *P*–*E* and *I*–*E* curves, respectively. Thus, at the phase transition temperature, the *h*-$DyFeO_3$ film exhibited FE

and AFE behaviors at low and high frequencies, respectively.

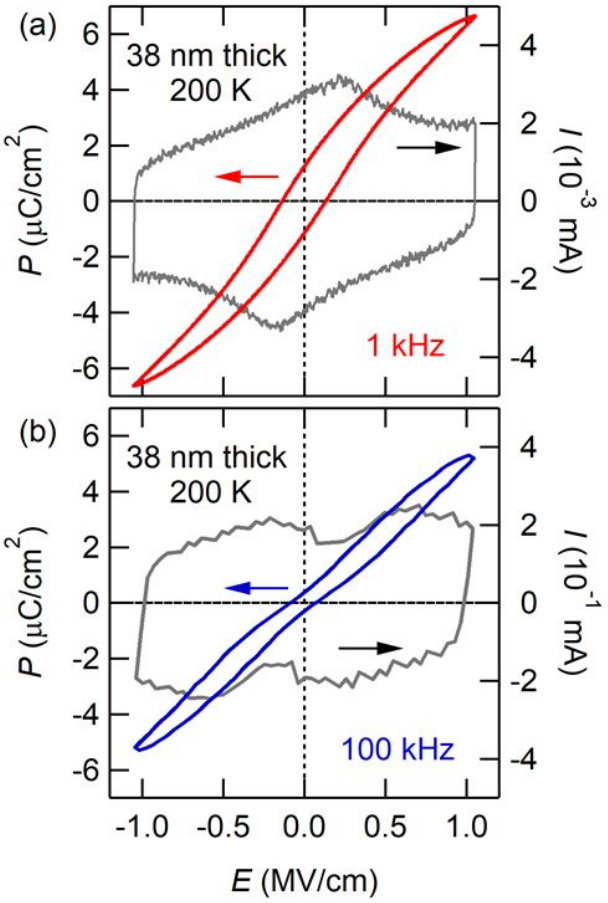

Figure 3. *P*–*E* and *I*–*E* curves for the 38-nm-thick *h*-$DyFeO_3$ film at (a) 1 and (b) 100 kHz at 200 K.

We also performed ferroelectric measurements for the 26- and 58-nm-thick *h*-$DyFeO_3$ films. The latter underwent a *T*-induced AFE–FE transition at 175 K (Fig. S7), The transition temperature is lower than that for the 38-nm-thick film (200 K), presumably due to the larger *c*/*a* ratio of the 58-nm-thick film (Fig. 1(c)). Figure 4 shows the *P*–*E* and *I*–*E* curves for the 26-nm-thick *h*-$DyFeO_3$ film as a function of *T*. Below 100 K typical characteristics of AFE were detected: double-hysteresis loops in the *P*–*E* the curves (Fig. 4(a)) and two pairs of current peaks in the *I*–*E* curves (Fig. 4(b)). On the other hand, at $T = 175$–200 K, the double-hysteresis loops become insignificant in the *P*–*E* curves (Fig. 4(c)), and new peaks corresponding to E_c appear between the E_A and E_F peaks in the *I*–*E* curves (Fig. 4(d)), indicating the coexistence of AFE and FE phases at high *T*.

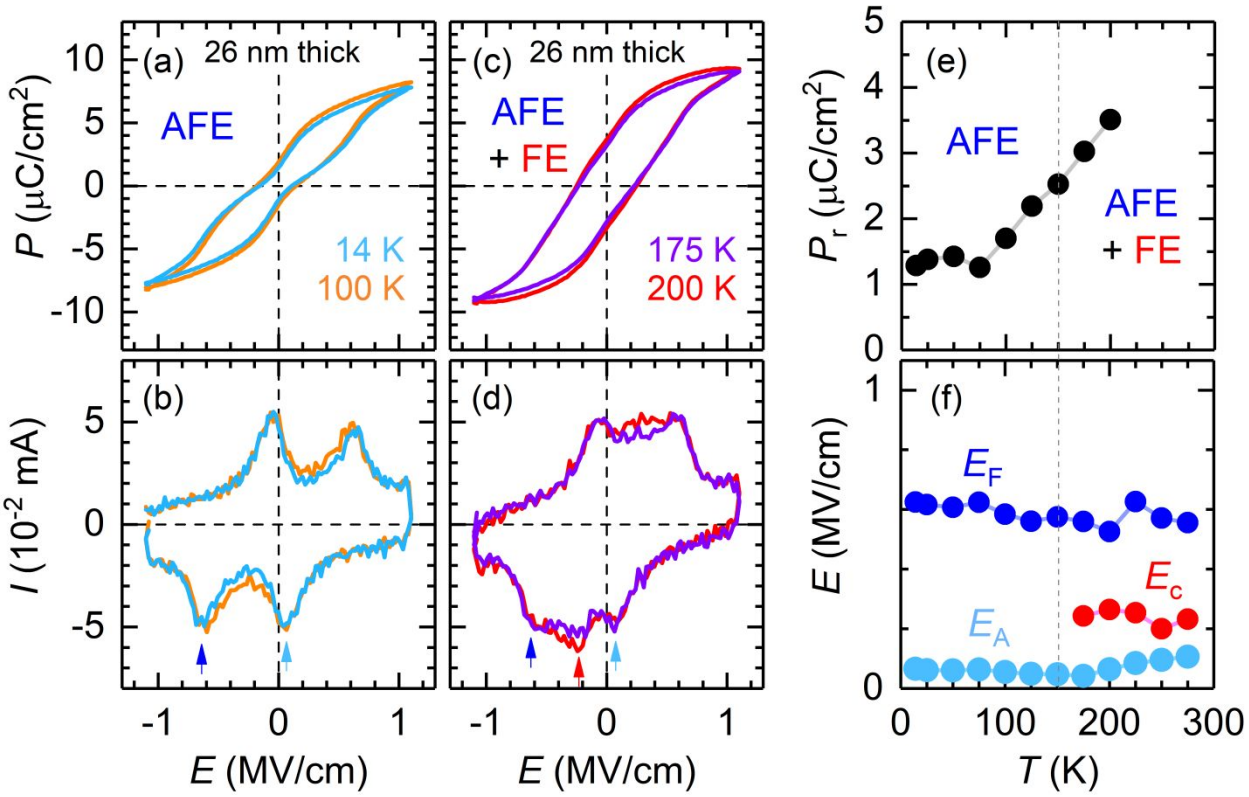

Figure 4. (a, b) *P*–*E* and (c, d) *I*–*E* curves for the 26-nm-thick *h*-$DyFeO_3$ film at (a, c) 14, 100, (b, d) 175, and 200 K at 10 kHz. *T* dependence of (e) P_r and (f) E_F, E_A, and E_c for the film with maximum applied *E* of 1.1 MV/cm.

Figure 4(e, f) shows the *T* dependence of P_r, E_A, E_F, and E_c for the 26-nm-thick *h*-$DyFeO_3$ film. With increasing *T*, the P_r values increased gradually from ~1.2 to 3.6 μC/cm^2 without a significant jump, suggesting that the volume fraction of the FE phase in the film increased gradually. The E_A and E_F values were almost constant at ~0.2 and 0.6 MV/cm, respectively. At *T* = 175–300 K, the E_c peak emerges and coexists with the E_A and E_F peaks, showing that the film consists of both AFE and FE phases within a wide range of *T* (175–300 K). This behavior is different from those of the 38- and 58-nm-thick *h*-$DyFeO_3$ films (Figs. 2 and S7). It is speculated that the coexistence of AFE and FE phases in the 26-nm-thick film is derived, not necessarily from a change in the *c*/*a* ratio, but from a change in the thickness. For example, it is expected that the contribution of the interface effect to the ferroelectric

properties increases with decreasing thickness. Indeed, in *h*-$YMnO_3$, it was reported that mechanical clamping by the substrate affects the build-up of primary-order trimerization, leading to a strong thickness dependence of the polarization [36]. However, further investigation is needed to elucidate the origin of the coexistence of the AFE and FE phases.

Figure 5 shows the FE and AFE phase diagram of *h*-*R*FeO_3 in terms of *c*/*a* and *T*. The figure does not include the results for the 26-nm-thick *h*-$DyFeO_3$ film because its ferroelectric properties are strongly related to the thickness effect. As shown in the figure, FE and AFE phases are related to *c*/*a* and *T*; increased *c*/*a* and *T* are conducive to triggering the FE phase. These results also suggest a possibility that the AFE–FE transition temperature could be adjusted to approximately room temperature via tuning the *c*/*a* ratio by changing the *R* ions and/or thickness.

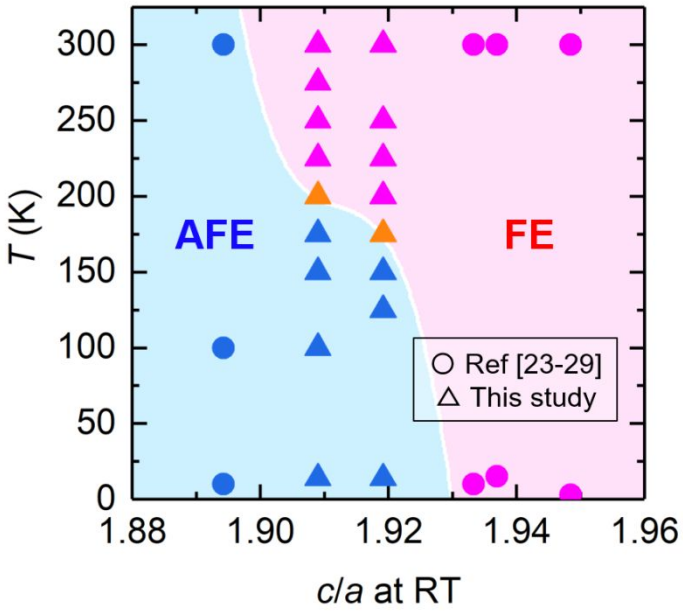

Figure 5. Phase diagram of *h*-*R*FeO_3 as a function of *c*/*a* ratio and *T*.

Antiferroelectric behavior has also been observed in *h*-*R*MnO_3, which is isostructural with *h*-*R*FeO_3, by decreasing the *c*/*a* value [9 -11]. L. H. Yin *et al*. investigated the origin of the AFE behavior in *h*-*R*MnO_3 by preparing single crystals of FE *h*-$YMnO_3$ and AFE Cr-doped *h*-$YMnO_3$ (*h*-YMCO)

[37]. Unlike conventional AFE materials such as $PbZrO_3$ [38] and $AgNbO_3$ [39], AFE *h*-YMCO has same crystal structure with FE *h*-$YMnO_3$. Thus, *E*-induced AFE–FE transition in *h*-YMCO is not accompanied with a crystal structure transition. The important difference between *h*-$YMnO_3$ and *h*-YMCO was observed in their unique topological domain structures. AFE *h*-YMCO has type-I domain pattern, while FE *h*-$YMnO_3$ consists of type-II one. The type-I domain pattern contains roughly equal fraction of upward and downward FE domains (P_{up} and P_{down}), resulting in zero net macroscopic *P*. Thus, the AFE behavior in *h*-YMCO is strongly related to the domain wall (DW) motion. As one of its unique features, it was reported that AFE behavior gradually disappears at low frequencies [37]. Such topological domain structures have been observed only in bulk single crystals [37, 40, 41]. Indeed, we could not observe such topological domain structures in the *h*-$DyFeO_3$ films using piezoresponse force microscopy technique (Fig. S9). For the observation of domain structures of the film, preparation of much thicker film may be needed. However, considering that AFE *h*-$DyFeO_3$ has polar crystal structure [24] and the AFE behavior gradually disappears at low frequency (Fig. 3), it is suggested that AFE behavior of the *h*-$DyFeO_3$ film is also strongly related to the DW motion. Our experimental results show that there are three factors that influence the AFE–FE transition of *h*-*R*FeO_3 films: *c*/*a*, *T*, and frequency, listed in the order of significance. *T* and frequency are related to migration length of DW. Indeed, in FE *h*-$ErMnO_3$, an increase in P_r and a decrease in E_c were observed when *T* increased or frequency decreased, due to an increase in migration length of DW [42]. On the other hand, when *c*/*a* is small, the ferroelectric domain size decreased in the initial state as previously reported [24], which probably results in an increase of the DW pinning centers and a resultant slow DW motion. It is noted that small *c*/*a*, which is obtained when lattice constant parallel (perpendicular) to polarization decreases (increases), tends to reduce the DW formation energy [43, 44].

5. Conclusion

In this study, we systematically investigated ferroelectric properties of the *h*-$DyFeO_3$ films by

controlling the *c*/*a* ratio in the range of 1.90–1.92, which is intermediate between those of previously reported AFE and FE *h*-*R*FeO_3. As a result, we successfully observed *T*-induced AFE–FE phase transition in the films. The AFE phase tends to stabilize at small *c*/*a* ratios and low temperatures. Additionally, the coexistence of AFE and FE was observed in the thinner films at room temperature.

Acknowledgments

This work was supported by JST, PRESTO Grant Number JPMJPR21Q3, Japan, JSPS KAKENHI (20H02614 (TK)) and Iketani Science and Technology Foundation (T.K.). H.O. was supported by Grant-in-Aid for Scientific Research on Innovative Areas (19H05791) from the JSPS. A part of this work was supported by Hokkaido University microstructural characterization platform as a program of "Nanotechnology Platform" of the Ministry of Education, Culture, Sports, Science and Technology (MEXT), Japan.

Supporting information

See supporting information for details of the crystal structures, chemical composition, and ferroelectric properties of the films.

References

[1] Hoffmann, M.; Schroeder, U.; Künneth, C.; Kersch, A.; Starschich, S.; Böttger, U.; Mikolajick, T., Ferroelectric phase transitions in nanoscale HfO_2 films enable giant pyroelectric energy conversion and highly efficient supercapacitors. *Nano Energy* **2015**, *18*, 154-164.

[2] Ahmed, A.; Goldthorpe, I. A.; Khandani, A. K., Electrically tunable materials for microwave applications. *Appl. Phys. Rev.* **2015**, *2*, 011302.

[3] Ustinov, A. B.; Kalinikos, B. A.; Srinivasan, G., Nonlinear multiferroic phase shifters for

microwave frequencies. *Appl. Phys. Lett.* **2014**, 104, 052911.

[4] Chiba, D.; Fukami, S.; Shimamura, K.; Ishiwata, N.; Kobayashi, K.; Ono, T., Electrical control of the ferromagnetic phase transition in cobalt at room temperature. *Nat. Mater.* **2011**, *10*, 853-856.

[5] Yamada, Y.; Ueno, K.; Fukumura, T.; Yuan, H.; Shimotani, H.; Iwasa, Y.; Gu, L.; Tsukimoto, S.; Ikuhara, Y.; Kawasaki, M., Electrically induced ferromagnetism at room temperature in cobalt-doped titanium dioxide. *Science* **2011**, 332, 1065-1067.

[6] Kim, K. D.; Lee, Y. H.; Gwon, T.; Kim, Y. J.; Kim, H. J.; Moon, T.; Hyun, S. D.; Park, H. W.; Park, M. H.; Hwang, C. S., Scale-up and optimization of HfO_2-ZrO_2 solid solution thin films for the electrostatic supercapacitors. *Nano Energy* **2017**, *39*, 390-399.

[7] Zhai, J.; Chen, H., Direct current field and temperature dependent behaviors of antiferroelectric to ferroelectric switching in highly (100)-oriented $PbZrO_3$ thin films. *Appl. Phys. Lett.* **2003**, *82*, 2673-2675.

[8] Kan, D.; Pálová, L.; Anbusathaiah, V.; Cheng, C. J.; Fujino, S.; Nagarajan, V.; Rabe, K. M.; Takeuchi, I., Universal behavior and electric-field-induced structural transition in rare-earth-substituted $BiFeO_3$. *Adv. Funct. Mater.* **2010**, *20*, 1108-1115.

[9] Murugavel, P.; Lee, J. H.; Lee, D.; Noh, T. W.; Jo, Y.; Jung, M.-H.; Oh, Y. S.; Kim, K. H., Physical properties of multiferroic hexagonal $HoMnO_3$ thin films. *Appl. Phys. Lett.* **2007**, *90*, 142902.

[10] Lee, J. H.; Murugavel, P.; Ryu, H.; Lee, D.; Jo, J. Y.; Kim, J. W.; Kim, H. J.; Kim, K. H.; Jo, Y.; Jung, M. H.; Oh, Y. H.; Kim, Y. W.; Yoon, J. G.; Chung, J. S.; Noh, T. W., Epitaxial stabilization of a new multiferroic hexagonal phase of $TbMnO_3$ thin films. *Adv. Mater.* **2006**, 18, 3125-3129.

[11] Lee, J. H.; Murugavel, P.; Lee, D.; Noh, T. W.; Jo, Y.; Jung, M. H.; Jang, K. H.; Park, J. G., Multiferroic properties of epitaxially stabilized hexagonal $DyMnO_3$ thin films. *Appl. Phys. Lett.* **2007**, *90*, 012903.

[12] Kouvel, J. S.; Hartelius, C. C., Anomalous Magnetic moments and transformations in the ordered alloy FeRh. *J. Appl. Phys.* **1962**, 33, 1343-1344.

[13] Stamm, C.; Thiele, J. U.; Kachel, T.; Radu, I.; Ramm, P.; Kosuth, M.; Minár, J.; Ebert, H.; Dürr, H. A.; Eberhardt, W.; Back, C. H., Antiferromagnetic-ferromagnetic phase transition in FeRh probed by X-ray magnetic circular dichroism. *Phys. Rev. B* **2008**, *77*, 184401.

[14] Ivanov, V. Y.; Mukhin, A. A.; Prokhorov, A. S.; Balbashov, A. M., Phase transitions in $Sm_{1-x}Sr_xMnO_3$ single crystals ($0 \leq x \leq 0.8$). *Phys. Status Solidi B* **2003**, 236, 445-449.

[15] Taskin, A. A.; Lavrov, A. N.; Ando, Y., Ising-like spin anisotropy and competing antiferromagnetic-ferromagnetic orders in $GdBaCo_2O_{5.5}$ single crystals. *Phys. Rev. Lett.* **2003**, *90*, 227201.

[16] Katayama, T.; Chikamatsu, A.; Zhang, Y.; Yasui, S.; Wadati, H.; Hasegawa, T., Ionic order engineering in double-perovskite cobaltite. *Chem. Mater*. **2021**, 33, 5675-5680.

[17] Hao, X.; Zhai, J., Electric-field tunable electrocaloric effects from phase transition between antiferroelectric and ferroelectric phase. *Appl. Phys. Lett.* **2014**, *104*, 022902.

[18] Xu, Z.; Zhai, J.; Chan, W. H., Phase transformation and electric field tunable pyroelectric behavior of $Pb(Nb,Zr,Sn,Ti)O_3$ and $(Pb,La)(Zr,Sn,Ti)O_3$ antiferroelectric thin films. *Appl. Phys. Lett*. **2006**, *88*, 132908.

[19] Naito, T.; Suzuki, I.; Itoh, M.; Taniyama, T., Effect of spin polarized current on magnetic phase transition of ordered FeRh wires. *J. Appl. Phys.* **2011**, *109*, 07C911.

[20] Li, M.; Tan, H.; Duan, W., Hexagonal rare-earth manganites and ferrites: a review of improper ferroelectricity, magnetoelectric coupling, and unusual domain walls. *Phys. Chem. Chem. Phys*. **2020**, *22*, 14415-14432.

[21] Das, H.; Wysocki, A. L.; Geng, Y.; Wu, W.; Fennie, C. J., Bulk magnetoelectricity in the hexagonal manganites and ferrites. *Nat. Commun*. **2014**, *5*, 2998.

[22] Wang, W.; Zhao, J.; Wang, W.; Gai, Z.; Balke, N.; Chi, M.; Lee, H. N.; Tian, W.; Zhu, L.;

Cheng, X.; Keavney, D. J.; Yi, J.; Ward, T. Z.; Snijders, P. C.; Christen, H. M.; Wu, W.; Shen, J.; Xu, X., Room-temperature multiferroic hexagonal $LuFeO_3$ films. *Phys. Rev. Lett*. **2013**, 110, 237601.

[23] Jeong, Y. K.; Lee, J. H.; Ahn, S. J.; Song, S. W.; Jang, H. M.; Choi, H.; Scott, J. F., Structurally tailored hexagonal ferroelectricity and multiferroism in epitaxial $YbFeO_3$ thin-film heterostructures. *J. Am. Chem. Soc.* **2012**, *134*, 1450-1453.

[24] Kasahara, J.; Katayama, T.; Mo, S.; Chikamatsu, A.; Hamasaki, Y.; Yasui, S.; Itoh, M.; Hasegawa, T., Room-temperature antiferroelectricity in multiferroic hexagonal rare-earth ferrites. *ACS Appl. Mater. Inter.* **2021**, *13*, 4230-4235.

[25] Bossak, A. A.; Graboy, I. E.; Gorbenko, O. Y.; Kaul, A. R.; Kartavtseva, M. S.; Svetchnikov, V. L.; Zandbergen, H. W., XRD and HREM studies of epitaxially stabilized hexagonal orthoferrites $RFeO_3$ (R = Eu− Lu). *Chem. Mater*. **2004**, 16, 1751-1755.

[26] Jeong, Y. K.; Lee, J.-H.; Ahn, S.-J.; Jang, H. M., Epitaxially constrained hexagonal ferroelectricity and canted triangular spin order in $LuFeO_3$ thin films. *Chem. Mater.* **2012**, 24, 2426-2428.

[27] Hamasaki, Y.; Katayama, T.; Yasui, S.; Shiraishi, T.; Akama, A.; Kiguchi, T.; Taniyama, T.; Itoh, M., Switchable third $ScFeO_3$ polar ferromagnet with $YMnO_3$-type structure. *J. Mater. Chem. C* **2020**, *8*, 4447-4452.

[28] Ahn, S.-H.; Lee, J.-H.; Jeong, Y. K.; Na, E.-H.; Koo, Y. M.; Jang, H. M. Artificially imposed hexagonal ferroelectricity in canted antiferromagnetic $YFeO_3$ epitaxial thin films. *Mater. Chem. Phys.* **2013**, *138*, 929−936.

[29] Ahn, S.-J.; Lee, J.-H.; Jang, H. M.; Jeong, Y. K. Multiferroism in hexagonally stabilized $TmFeO_3$ thin films below 120 K. *J. Mater. Chem. C* **2014**, 2, 4521−4525.

[30] Ohta, H.; Orita, M.; Hirano, M.; Hosono, H. Surface morphology and crystal quality of low resistive indium tin oxide grown on yittria-stabilized zirconia. *J. Appl. Phys.* **2002**, 91, 3547-

3550.

[31] Ohta, H.; Kambayashi, T.; Hirano, M.; Hoshi, H.; Ishikawa, K.; Takezoe, H.; Hosono, H. Application of a transparent conductive substrate with an atomically flat and stepped surface to lateral growth of an organic molecule: vanadyl phthalocyanine. *Adv. Mater.* **2003**, *15*, 1258-1262.

[32] Luo, S.; Fluri, A.; Zhang, S.; Liu, X.; Döbeli, M.; Harrington, G. F.; Tu, R.; Pergolesi, D.; Ishihara, T.; Lippert, T., Thickness-dependent microstructural properties of heteroepitaxial (00.1) $CuFeO_2$ thin films on (00.1) sapphire by pulsed laser deposition. *J. Appl. Phys.* **2020,** *127*, 065301.

[33] Rachut, K.; Bayer, T. J. M.; Wolff, J. O.; Kmet, B.; Benčan, A.; Klein, A., Off-stoichiometry of magnetron sputtered $Ba_{1-x}Sr_xTiO_3$ thin films. *Phys. Status Solidi B* **2019,** 256, 1900148.

[34] Disseler, S. M.; Borchers, J. A.; Brooks, C. M.; Mundy, J. A.; Moyer, J. A.; Hillsberry, D. A.; Thies, E. L.; Tenne, D. A.; Heron, J.; Holtz, M. E.; Clarkson, J. D.; Stiehl, G. M.; Schiffer, P.; Muller, D. A.; Schlom, D. G.; Ratcliff, W. D., Magnetic structure and ordering of multiferroic hexagonal $LuFeO_3$. *Phys. Rev. Lett.* **2015**, 114, 217602.

[35] Moyer, J. A.; Misra, R.; Mundy, J. A.; Brooks, C. M.; Heron, J. T.; Muller, D. A.; Schlom, D. G.; Schiffer, P., Intrinsic magnetic properties of hexagonal $LuFeO_3$ and the effects of nonstoichiometry. *APL Mater*. **2014**, *2*, 012106.

[36] Nordlander, J.; Campanini, M.; Rossell, M. D.; Erni, R.; Meier, Q. N.; Cano, A.; Spaldin, N. A.; Fiebig, M.; Trassin, M., The ultrathin limit of improper ferroelectricity. *Nat. Commun.* **2019,** *10*, 5591.

[37] Yin, L. H.; Yang, J. F.; Zhang, R. R.; Yang, J.; Tong, P.; Song, W. H.; Dai, J. M.; Zhu, X. B.; Sun, Y. P., Topological domain-engineered antiferroelectric-like behavior with enhanced energy storage properties in ferroelectric hexagonal Cr-doped $YMnO_3$. *Ceram. Int.* **2019,** *45*, 20276-20281.

[38] Shirane, G.; Sawaguchi, E.; Takagi, Y., Dielectric properties of lead zirconate. *Phys. Rev.* **1951,** *84*, 476-481.

[39] Sciau, P.; Kania, A.; Dkhil, B.; Suard, E.; Ratuszna, A., Structural investigation of $AgNbO_3$ phases using X-ray and neutron diffraction. *J. Phys.: Condens. Matter.* **2004,** *16*, 2795-2810.

[40] Du, K.; Gao, B.; Wang, Y.; Xu, X.; Kim, J.; Hu, R.; Huang, F.-T.; Cheong, S.-W., Vortex ferroelectric domains, large-loop weak ferromagnetic domains, and their decoupling in hexagonal (Lu, Sc)FeO_3. *npj Quantum Mater.* **2018,** *3*, 33.

[41] Chae, S. C.; Horibe, Y.; Jeong, D. Y.; Rodan, S.; Lee, N.; Cheong, S. W., Self-organization, condensation, and annihilation of topological vortices and antivortices in a multiferroic. *Proc. Natl. Acad. Sci. U.S.A.* **2010,** *107*, 21366-70.

[42] Ruff, A.; Li, Z.; Loidl, A.; Schaab, J.; Fiebig, M.; Cano, A.; Yan, Z.; Bourret, E.; Glaum, J.; Meier, D.; Krohns, S., Frequency dependent polarisation switching in *h*-$ErMnO_3$. *Appl. Phys. Lett.* **2018,** *112* 182908.

[43] Samanta, A.; Yadav, S.; Gu, Z.; Meyers, C. J. G.; Wu, L.; Chen, D.; Pandya, S.; York, R. A.; Martin, L. W.; Spanier, J. E.; Grinberg, I., A predictive theory for domain walls in oxide ferroelectrics based on interatomic interactions and its implications for collective material properties. *Adv. Mater.* **2021**, 2106021.

[44] Cohen, R. E., Origin of ferroelectricity in perovskite oxides. *Nature* **1992,** *358*, 136-138.